9-1-2020

High MB solution degradation efficiency of FeSiBZr amorphous ribbon with surface tunnels

Qi Chen

Zhicheng Yan

Hao Zhang

Lai-Chang Zhang
Edith Cowan University

Haijian Ma

See next page for additional authors

10.3390/MA13173694

Chen, Q., Yan, Z., Zhang, H., Zhang, L. C., Ma, H., Wang, W., & Wang, W. (2020). High MB Solution Degradation Efficiency of FeSiBZr Amorphous Ribbon with Surface Tunnels. Materials, 13(17), 3694. https://doi.org/10.3390/MA13173694

materials

MDPI

Article

High MB Solution Degradation Efficiency of FeSiBZr Amorphous Ribbon with Surface Tunnels

Qi Chen [1], Zhicheng Yan [1], Hao Zhang [1], Lai-Chang Zhang [2], Haijian Ma [3], Wenlong Wang [4] and Weimin Wang [1,*]

1 Key Laboratory for Liquid-Solid Structural Evolution and Processing of Materials (Ministry of Education), School of Materials Science and Engineering, Shandong University, Jinan 250061, China; caesar@mail.sdu.edu.cn (Q.C.); rengaryzc@outlook.com (Z.Y.); zhanghao_0611@163.com (H.Z.)

2 School of Engineering, Edith Cowan University, 270 Joondalup Drive, Joondalup, Perth WA6027, Australia; l.zhang@ecu.edu.au

3 School of Mechanical, Electrical and Vehicle Engineering, Weifang Institute, Weifang 261061, China; hjma@wfu.edu.cn

4 National Engineering Laboratory for Reducing Emissions from Coal Combustion, Engineering Research Center of Environmental Thermal Technology of Ministry of Education, Shandong Key Laboratory of Energy Carbon Reduction and Resource Utilization, School of Energy and Power Engineering, Shandong University, Jinan 250061, China; wwenlong@sdu.edu.cn

* Correspondence: weiminw@sdu.edu.cn; Tel.: +86-531-8839-2749

Received: 24 July 2020; Accepted: 13 August 2020; Published: 21 August 2020

Abstract: The as spun amorphous $(Fe_{78}Si_9B_{13})_{99.5}Zr_{0.5}$ (Zr0.5) and $(Fe_{78}Si_9B_{13})_{99}Zr_1$ (Zr1) ribbons having a Fenton-like reaction are proved to bear a good degradation performance in organic dye wastewater treatment for the first time by evaluating their degradation efficiency in methylene blue (MB) solution. Compared to the widely studied $(Fe_{78}Si_9B_{13})_{100}Zr_0$ (Zr0) amorphous ribbon for degradation, with increasing c_{Zr} (Zr atomic content), the as-spun Zr0, Zr0.5 and Zr1 amorphous ribbons have gradually increased degradation rate of MB solution. According to δ_c (characteristic distance) of as-spun Zr0, Zr0.5 and Zr1 ribbons, the free volume in Zr1 ribbon is higher Zr0 and Zr0.5 ribbons. In the reaction process, the Zr1 ribbon surface formed the 3D nano-porous structure with specific surface area higher than the cotton floc structure formed by Zr0 ribbon and coarse porous structure formed by Zr0.5 ribbon. The Zr1 ribbon's high free volume and high specific surface area make its degradation rate of MB solution higher than that of Zr0 and Zr0.5 ribbons. This work not only provides a new method to remedying the organic dyes wastewater with high efficiency and low-cost, but also improves an application prospect of Fe-based glassy alloys.

Keywords: Fe-based alloys; methylene blue dye; free volume; surface tunnel

1. Introduction

Nowadays, organic dyes wastewater is commonly produced in the industrial production of dyestuff, textiles, paper and plastics. This organic dyes wastewater contains carcinogenic, teratogenic and biological toxic substances, which will cause serious pollution to the environment [1–3]. Thus, increasing attention has been paid to the harmful pollution of industrial organic dyes to our water bodies. In the past several decades, numerous research works have been done to reduce their hazardous effects, including the physical adsorption of activated carbon and clay [4,5], biodegradation [6], chemical degradation by advanced oxidation process [7–10] and degradation of specific alloys [11–14]. However, these methods have obvious disadvantages such as low-efficiency, high-cost and short service life. Thus, we should actively explore advanced materials to better degrade organic dyes in polluted water [15].

Amorphous alloys (metallic glass alloys) have excellent properties such as high strength and corrosion resistance due to their long-range disordered atomic structures, and the importance of fundamental scientific and engineering application potential is attracting rising attention [16–18]. At present, the amorphous alloy ribbons including Mg-based ribbons [19–23], Al-based ribbons [24–26], Co-based ribbons [27–29] and Fe-based ribbons [30–36] have been proved to have good degradation properties to organic dyes wastewater. It is well-believed that the excellent degradation ability of amorphous alloys is due to three factors: (1) their high residual stress, (2) thermodynamic instabilityand (3) lots of unsaturated sites on the surface.

Among Fe-, Cu-, Al- and Mg-based amorphous alloys used to degrade organic dyes wastewater, Fe-based alloys have attracted the most attention because of their high degradation efficiency, low cost and good reusability. The frequently used Fe-based alloys for degradation are FeSiB systems, and FeSiB alloys with other elements. Jia et al., using the prepared $Fe_{78}Si_9B_{13}$ and $Fe_{73.5}Si_{13.5}B_9Cu_1Nb_3$ amorphous ribbons, showed higher degradation efficiency when degrading cibacron brilliant red 3B-A, methyl blue and methyl orange dyes by Fenton-like reaction ($Fe^0 + H_2O_2 \rightarrow Fe^{2+} + 2OH^-$, $Fe^{2+} + H_2O_2 \rightarrow Fe^{3+} + \cdot\bullet OH + OH^-$, $\bullet OH$ + organics → products), which proved that Fe-based amorphous ribbons have better degradation performance of organic dyes than other kinds of amorphous alloys [37,38]. Xie et al. used amorphous $Fe_{76}Si_9B_{12}Y_3$ powder to degrade methyl orange dye, which was 1000 times more reactive than industrial iron powder [39].

In this paper, using $(Fe_{78}Si_9B_{13})_{99.5}Zr_{0.5}$ (Zr0.5) and $(Fe_{78}Si_9B_{13})_{99}Zr_1$ (Zr1) amorphous ribbons, the methylene blue (MB) dyes degradation by Fenton-like reactions is reported for the first time, and is compared with $Fe_{78}Si_9B_{13}$ (Zr0) amorphous ribbon. The addition of trace Zr element effectively adjusts the interatomic force of Zr0 amorphous ribbon, which makes the atoms on the surface of amorphous ribbon participate in Fenton-like reaction more easily, and with the increase of Zr element content, it is easier to form developed 3D nano-porous acicular structure on the ribbon surface, thus increasing the specific surface area of reaction and improving the degradation rate. The effects of initial pH and H_2O_2 concentration on the degradation efficiency of MB using the Zr0, Zr0.5 and Zr1 amorphous ribbons during Fenton-like reactions are investigated. This work not only provides a new routine for the remediation of organic dyes wastewater, but also extends the application range of Fe-based amorphous/glassy alloys.

2. Experimental

2.1. Materials and Reagent

Alloy ingots with a nominal composition of $(Fe_{78}Si_9B_{13})_{100}Zr_0$ (Zr0, at.%), $(Fe_{78}Si_9B_{13})_{99.5}Zr_{0.5}$ (Zr0.5, at.%) and $(Fe_{78}Si_9B_{13})_{99}Zr_1$ (Zr1, at.%) were prepared by arc melting of pre-alloyed $Fe_{78}Si_9B_{13}$ ingots and high-purity Zr (99.99 wt.%) in an arc melting furnace (MAM-1 Edmund Buhler, Berlin, Germany), which was vacuumed to 5×10^{-3} Pa first and then filled with purified argon (99.999%). The ribbons with thickness of ~30 μm and width of ~2.5 mm were prepared by single copper roller melt-spinning (i.e., planar flow casting) system. The roller/wheel speed was 42 $m \cdot s^{-1}$. The amorphous ribbons were cut into 5 cm long strips for degradation tests. Commercially available methylene blue (MB, $C_{16}H_{18}ClN_3S$, AR grade, Tianjin Beichen Fangzheng Reagent Factory, Tianjin, China), Hydrochloric acid (HCl, AR grade, Sinopharm Chemical Reagent Co., Ltd., Shanghai, China), Sodium hydroxide (NaOH, AR grade, Tianjin Hengxing Chemical Reagent Manufacturing Co., Ltd., Tianjin, China) and Hydrogen peroxide (H_2O_2, AR grade, Tianjin Kemeo Chemical Reagent Co., Ltd. Tianjin, China) are used in the experiment.

2.2. Characterization

The amorphous structure of the as-spun ribbons (in a stripe-like shape) was investigated by X-ray diffraction (XRD, Bruker D8 Discover, Brooke (Beijing) Technology Co., Ltd., Beijing, China) with Cu-Kα radiation and transmission electron microscopy (TEM, FEI Tecnai G2 F20, American FEI

Company, Portland, OR, America). The amorphous character of the ribbon samples was also confirmed by differential scanning calorimetry (DSC, Netzsch-404, Netzsch, Bavaria, Germany) at a heating rate of 20 K/min. The surface morphology of the as-spun and reacted ribbons was observed by scanning electron microscope (SEM, JSM-7800F, Japan Electronics Co., Ltd., Beijing, China) equipped with an energy dispersive X-ray spectrometer (EDS).

2.3. Degradation Tests

Preparing MB solution in 500 mL volumetric flask with deionized water (DW), then pour 100 mL MB solution (100 mg L^{-1}) in 250 mL beakers. A certain mass of ribbons (0.5 g L^{-1}) and H_2O_2 (1 mM) was placed to the MB solution, stirring at a fixed speed (300 r min^{-1}) during the degradation process, and the constant temperature (298 K) of the MB solution was maintained with a water bath. The pH (pH = 3) of the MB solution was adjusted using 12 mol L^{-1} HCl, as well as 1 M NaOH. At time intervals, a 3 mL solution was extracted with a syringe and filtered with a 0.45 μm membrane, and the concentration of MB solution was monitored in real-time with UV-Vis spectrophotometer (UV-4802) to obtain the absorbance spectrum of the solution.

2.4. Electrochemical Tests

The polarization curves and electrochemical impedance spectra (EIS) were measured using an electrochemical measuring instrument (CHI 660E, Shanghai Chenhua Instrument Co., Ltd., Shanghai, China) in the 20 mL DW or MB solutions (pH = 3, T = 298 K, C_{H2O2} = 1 mM and C_{MB} = 100 mg·L^{-1}). The three-electrode cell was used for measurement, the saturated calomel electrode (SCE) was used as reference electrode, platinum was used as counter electrode and as-spun ribbon was used as working electrode. When the open-circuit potential stabilizes, the polarization curve was recorded at the potential scanning speed of 1 mV s^{-1}. EIS was performed in static states, with scanning frequencies from 100 kHz to 0.01 Hz and the amplitude of ± 10 mV.

3. Results

3.1. XRD, DSC and TEM Analysis

Figure 1a shows the x-ray diffraction XRD curves of as-spun $(Fe_{78}Si_9B_{13})_{100}Zr_0$ (Zr0), $(Fe_{78}Si_9B_{13})_{99.5}Zr_{0.5}$ (Zr0.5) and $(Fe_{78}Si_9B_{13})_{99}Zr_1$ (Zr1) ribbons. The XRD curves of as-spun Zr0, Zr0.5 and Zr1 ribbons have only a typical diffuse scattering peak at $2\theta_{max}$ = 44.45°, 44.32° and 44.14° respectively, indicating that the as-spun Zr0, Zr0.5 and Zr1 ribbons owns a fully amorphous structure. With the increase of Zr content, the diffuse scattering peak moves to a low degree. The mean neighboring atomic distance increases with Zr content due to the large atom size of Zr element [40]. Figure 1b shows the DSC curves of as-spun Zr0, Zr0.5 and Zr1 ribbons. In the DSC curves of as-spun Zr0, Zr0.5 and Zr1 ribbons, there are two crystallization peak temperatures T_{P1} and T_{P2}, a melting peak temperature T_{P3} in the heating scan, respectively. The T_{P2}-T_{P1} (crystallization peak temperature range) of as-spun Zr0, Zr0.5 and Zr1 ribbons are 18, 41 and 68 K, respectively. Not only are the two crystallization peak temperatures T_{P1} and T_{P2} of as-spun Zr0.5 and Zr1 ribbons higher than that of as-spun Zr0 ribbon, but also their crystallization peak temperature range of T_{P2}-T_{P1} higher than that of as-spun Zr0 ribbon, indicating that the as-spun Zr0.5 and Zr1 ribbons have better amorphous stability and formability. The melting peak temperature T_{P3} of as-spun Zr0.5 and Zr1 ribbons was lower than that of as-spun Zr0 ribbon, indicating that the addition of Zr element can reduce the bonding force between atoms in amorphous ribbons, thus have a lower melting peak temperature.

In order to further characterize the microstructure of the as-spun Zr0, Zr0.5 and Zr1 ribbons, we conducted TEM investigations, which are shown in Figure 2. There is mainly maze shape pattern without crystallites in the high-resolution bright field images of the as-spun Zr0, Zr0.5 and Zr1 ribbons (Figure 2a–c), and the corresponding SAED (Selected area electron diffraction) patterns have two typical diffraction halos (Figure 2d–f), confirming that the as-spun Zr0, Zr0.5 and Zr1 ribbons own

a fully amorphous structure. Thus, the results of TEM are agreeing with the XRD curves and DSC curves (Figure 1a,b).

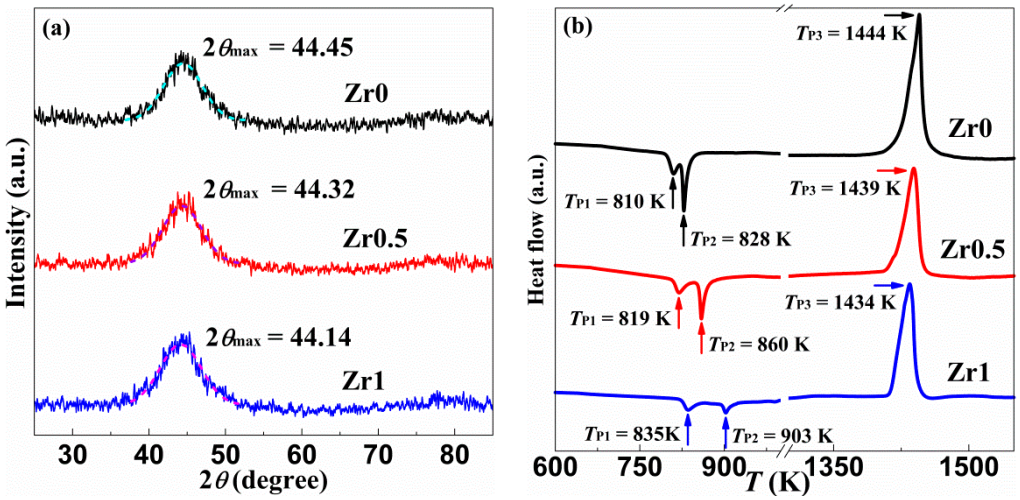

Figure 1. (**a**) The X-ray diffraction (XRD) curves of as-spun Zr0, Zr0.5 and Zr1 ribbons, (**b**) the differential scanning calorimetry (DSC) curves of the as-spun Zr0, Zr0.5 and Zr1 ribbons.

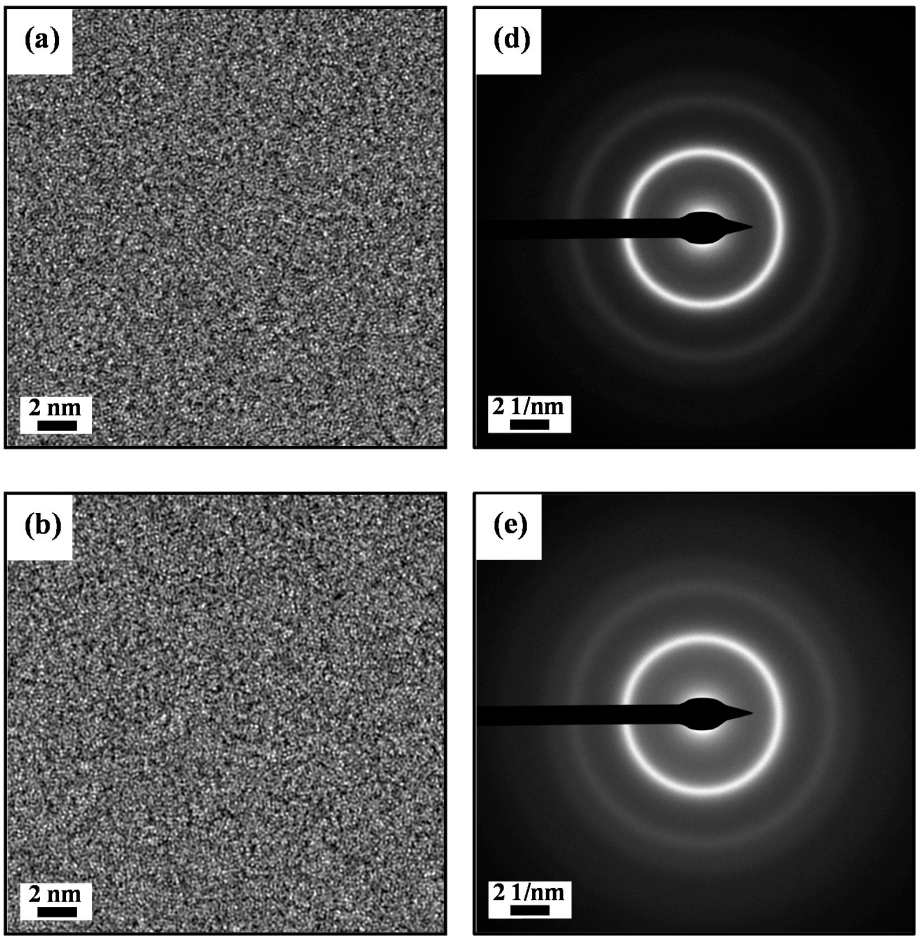

Figure 2. *Cont.*

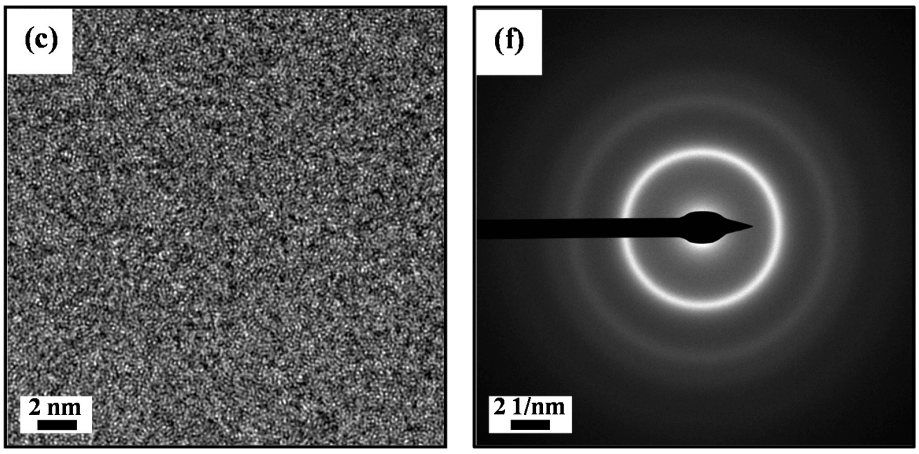

Figure 2. The transmission electron microscopy (TEM) images of the as-spun (**a**) Zr0, (**b**) Zr0.5 and (**c**) Zr1 ribbons, the SAED (Selected area electron diffraction)patterns of the as-spun (**d**) Zr0, (**e**) Zr0.5 and (**f**) Zr1 ribbons.

3.2. Degradation Performance

Figure 3a–c exhibits the ultraviolet–visible (UV–vis) absorption spectra of filtered methylene blue (MB) solution in a series of time intervals after adding the as-spun Zr0, Zr0.5 and Zr1 ribbons in the reaction batch, respectively. The UV–vis absorption spectra of MB solution have two major absorption peaks at about 610 nm and 654 nm, which represent the auxochrome and chromophore groups, respectively [38]. The normalized concentration of the MB solution obtains its peak value at 654 nm, which represents the chromogenic species, as shown in Figure 3d. With increasing t_r the absorption peak at 654 nm gradually decayed, indicating that the chromophore groups of MB disappeared gradually. In the first 9 min, the auxochrome groups react more quickly with Fe-based ribbons than the chromophore groups. The degradation kinetics is usually described by the pseudo-first-order equation as follows [41]:

$$C_t = C_0 \exp(-kt_r), \quad (1)$$

where k is the reaction rate constant (min^{-1}), C_0 is the initial concentration of MB solution (mg L^{-1}), t_r is the reaction time (min), and C_t is the instant concentration of MB solution (mg L^{-1}) at t_r. In this work, the ln (C_0/C_t) − t_r curves are shown in the inset of Figure 3d. The deduced k of as-spun Zr0.5 and Zr1 ribbons are 0.22 min^{-1} and 0.24 min^{-1}, which is larger than 0.19 min^{-1} for as-spun Zr0 ribbon. Here, the fit goodness values R^2 of Zr0, Zr0.5 and Zr1 ribbons are 0.97, 0.98 and 0.97, respectively. Thus, the as-spun Zr0.5 and Zr1 ribbons bear a higher degradation performance for MB solution compared with as-spun Zr0 ribbon.

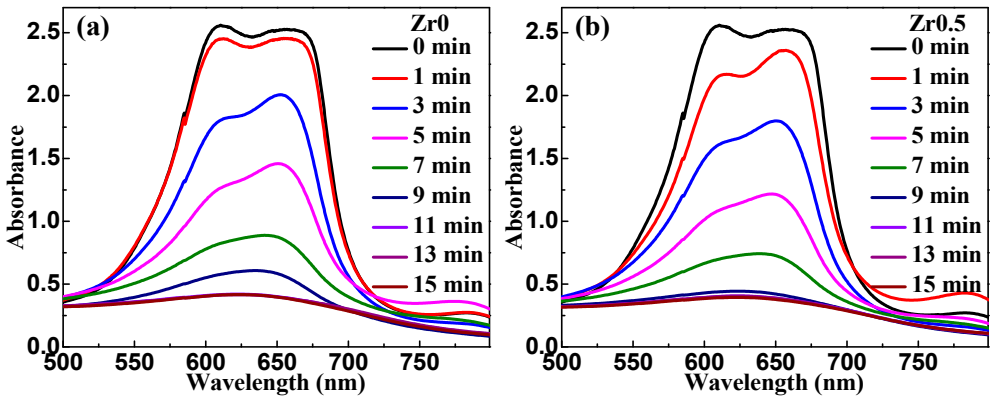

Figure 3. *Cont.*

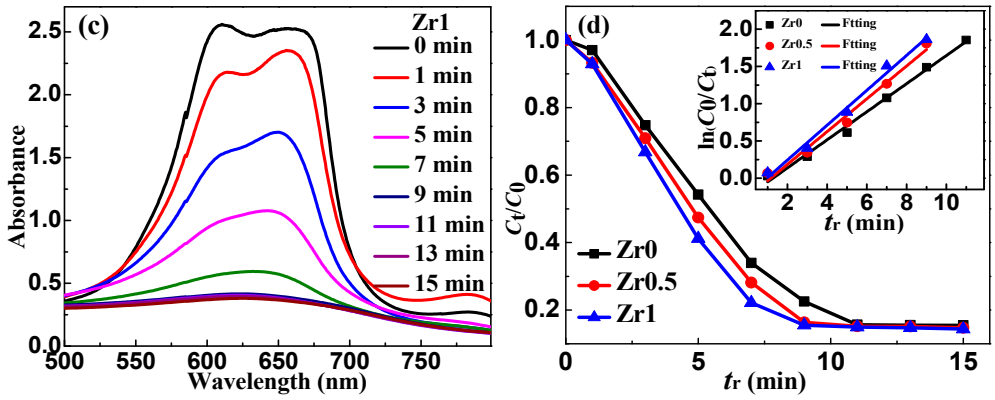

Figure 3. The ultraviolet–visible (UV–Vis) absorbance spectra of methylene blue (MB) solution during the Fenton-like reactions using as-spun (**a**) Zr0, (**b**) Zr0.5 and (**c**) Zr1 ribbons and (**d**) the normalized concentration change of MB solution during the degradation process. The inset in (**d**): the $\ln(C_0/C_t)$-t_r curves for as-spun Zr0, Zr0.5 and Zr1 ribbons (T = 298 K, pH = 3, $C_{H_2O_2}$ = 1 mM, ribbon dosage = 0.5 g L^{-1} and C_{MB} = 100 mg L^{-1}). Symbols show the experimental data while solid lines are fitting results.

3.3. Surface Morphology

In order to deeply understand the MB solution degradation mechanism with the Zr0, Zr0.5 and Zr1 amorphous ribbons, we test to study the structural evolution of the ribbon surfaces during the Fenton-like reaction process. The SEM images on the surface of the as-spun and reacted Zr0, Zr0.5 and Zr1 ribbons are displayed in Figure 4 and the EDS results are listed in Table 1. The as-spun Zr0, Zr0.5 and Zr1 ribbons have a typical smooth amorphous surface, as shown in Figure 4a–c, respectively. There are cotton floc structures and some corrosion pit on the reacted Zr0 ribbon (Figure 4d). The reacted Zr0.5 ribbon surface appears in coarse porous structure with the ligament width of 100 nm (Figure 4e). The reacted Zr1 ribbon surface has a developed 3D nano-porous structure with some acicular matters on the ligaments (Figure 4f). The porous surface structures should have enhancing effects on the degradation process because they can provide mass transfer channels. Compared with Zr0 and Zr0.5 ribbons, the higher pore density of Zr1 ribbon may be the reason for its higher degradation performance in Fenton-like reaction.

The XRD patterns of Zr0, Zr0.5 and Zr1 ribbons (upper right inset in Figure 4d–f) after reaction still have only a typical diffuse scattering peak at $2\theta_{max}$ = 44.56°, 44.47° and 44.39° respectively, indicating that they still own a fully amorphous structure. Here, the different peak positions of the reacted ribbons are higher than the as-spun ribbons. Moreover, the $2\theta_{max}$ deviation $\Delta 2\theta_{max}$ values of Zr0, Zr0.5 and Zr1 ribbons are 0.11°, 0.15° and 0.25°, respectively, showing a high tendency with increasing c_{Zr}. After reacting with MB solution for 15 min, the Zr0, Zr0.5 and Zr1 ribbons have a decreased c_{Fe}, and the c_{Zr} has remained basically unchanged. Moreover, the decrease of Fe element on the surface of Zr1 ribbon is higher than that of Zr0 and Zr0.5 ribbons, indicating that the high degradation rate of Zr1 ribbon is due to a large amount of Fe element participating in the Fenton-like reaction. After degradation, the c_O on Zr0, Zr0.5 and Zr1 ribbon surface increases, indicating that the degradation process involves the oxidation of the ribbons.

Table 1. Energy dispersive X-ray spectrometer (EDS) analysis of the Zr0, Zr0.5 and Zr1 ribbons before and after reacted (at.%).

Alloy	Before Reacted					After Reacted				
	c_{Fe}	c_{Si}	c_B	c_{Zr}	c_O	c_{Fe}	c_{Si}	c_B	c_{Zr}	c_O
Zr0	77.8	8.7	10.9	-	2.6	76.3	8.6	10.5	-	4.6
Zr0.5	75.5	7.9	13.0	0.7	2.9	62.1	7.1	11.3	0.8	18.7
Zr1	76.1	9.0	10.3	1.4	3.2	53.4	8.5	9.6	1.6	26.9

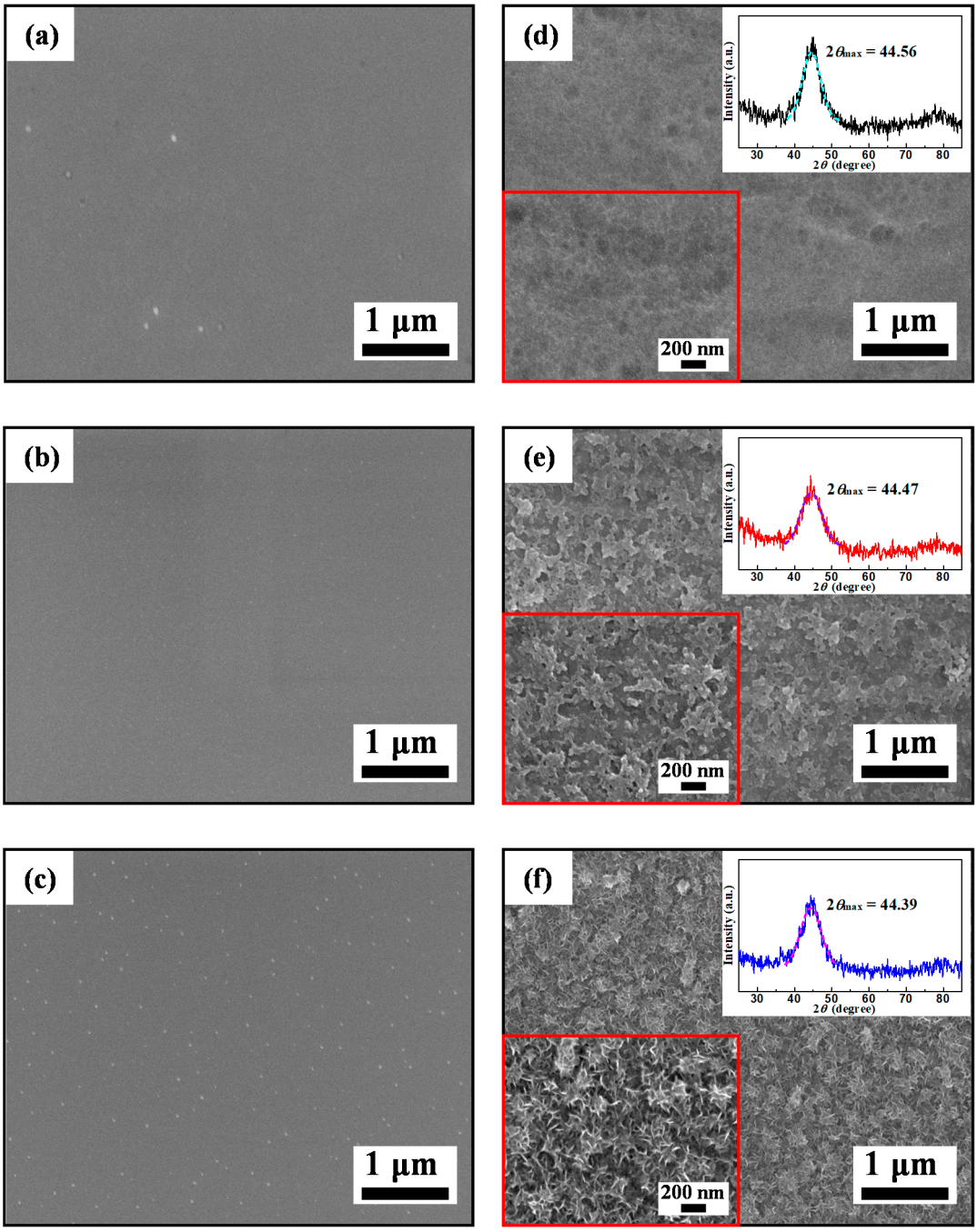

Figure 4. SEM micrographs of the as-spun (**a**) Zr0, (**b**) Zr0.5 and (**c**) Zr1 ribbons, and reacted (**d**) Zr0, (**e**) Zr0.5 and (**f**) Zr1 ribbons The insets in (**d**–**f**): the high-magnification images and XRD patterns of reacted Zr0, Zr0.5 and Zr1 ribbons.

3.4. Electrochemical Analysis

The polarization curves and electrochemical impedance spectra (EIS) of the as-spun Zr0, Zr0.5 and Zr1 ribbons in DW and MB solution (T = 298 K, pH = 3, C_{H2O2} = 1 mM and C_{MB} = 100 mg L^{-1}) are shown in Figure 5. In DW, the corrosion potentials (E_{corr}) of the Zr0.5 and Zr1 ribbons are −0.75 and −0.71 V (Figure 5a), higher than the Zr0 ribbon (−0.80 V). The corrosion current densities (i_{corr}) of the Zr0.5 and Zr1 ribbons are 5.83×10^{-6} and 3.30×10^{-6} A·cm^{-2}, lower than the Zr0 ribbon (8.23×10^{-6} A cm^{-2}). In MB solution, the E_{corr} of the Zr0.5 and Zr1 ribbons are −0.60 and −0.54 V (Figure 5b), higher than the Zr0 ribbon (−0.65 V). The i_{corr} of the Zr0.5 and Zr1 ribbons are 1.54×10^{-4} and 1.20×10^{-4} A cm^{-2},

lower than the Zr0 ribbon (1.82×10^{-4} A cm^{-2}). The above data from polarization curves indicate that the Zr0.5 and Zr1 ribbons have better corrosion resistance than the Zr0 ribbon in DW and MB solution.

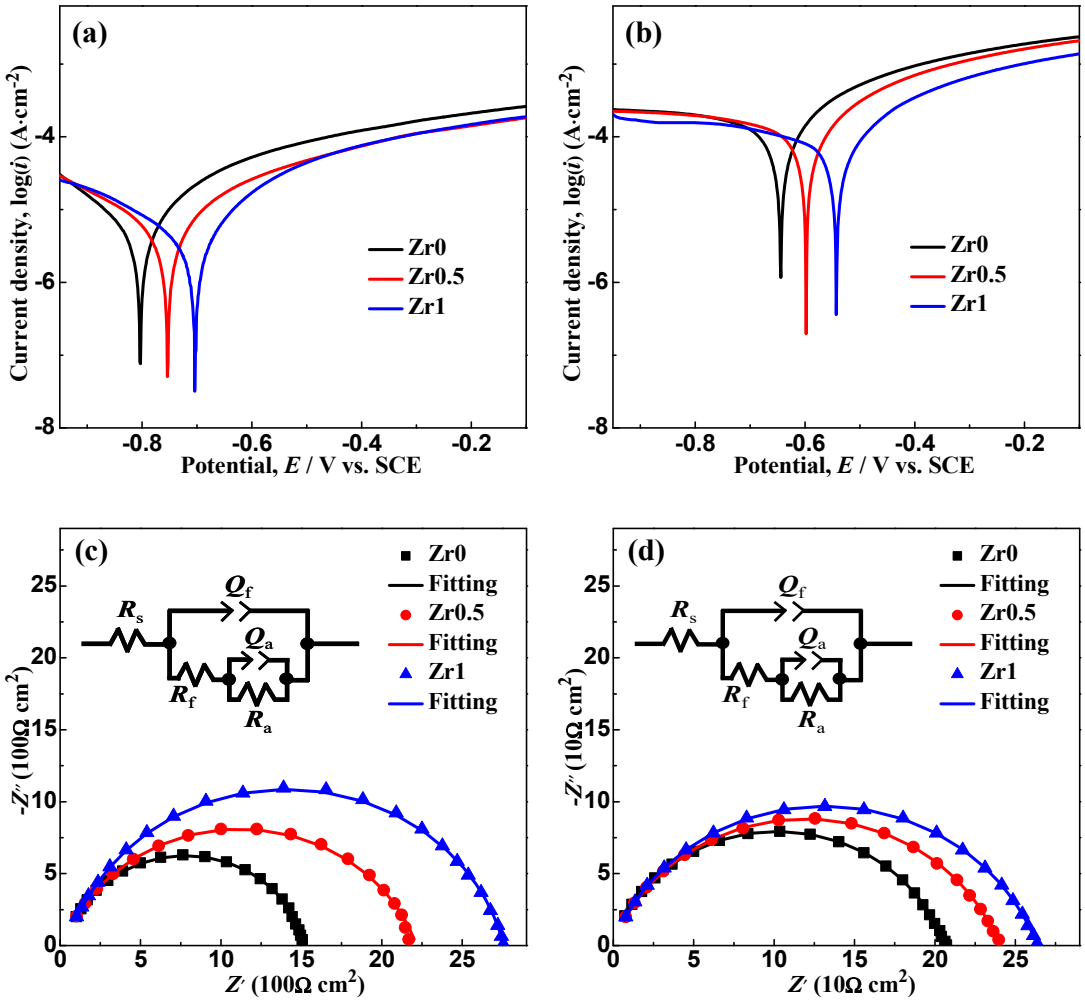

Figure 5. Polarization curves of the as-spun Zr0, Zr0.5 and Zr1 ribbons in (**a**) DW and (**b**) MB solution (T = 298 K, pH = 3, C_{H2O2} = 1 mM and C_{MB} = 100 mg L^{-1}) and their Nyquist curves in (**c**) DW and (**d**) MB solution. The insets in (**c**,**d**): the general fitted circuit. Symbols show the experimental data while solid lines are fitting results.

In both DW and MB solution (Figure 5c,d), the Nyquist semicircle diameter of the Zr0.5 and Zr1 ribbons is larger than that of Zr0 ribbon. The equivalent circuit composed of R(Q(R(QR))) is used to fit the EIS data. The fitting error (chi square χ^2) for the Zr0, Zr0.5 and Zr1 ribbons are 1.47×10^{-5}, 1.07×10^{-4} and 6.54×10^{-4} in DW, respectively; while they are 1.05×10^{-5}, 6.77×10^{-6} and 7.71×10^{-6} in MB solution, respectively. In the equivalent circuit, the phase element (CPE) Q is defined as [42]:

$$Q = (jw)^{-n}/Y_0, \quad (2)$$

where Q is the resistance, j is the imaginary unit, w is the frequency, n is the coefficient of CPE and Y_0 is the admittance.

The fitting results are summarized in Table 2. The R_s (solution resistance) of the Zr0, Zr0.5 and Zr1 ribbons in MB solution is lower than that in DW, which may be due to the conductive H^+ in MB solution. The R_f (resistance of passivation film) and R_a (resistance of electrochemical reaction) of the Zr0, Zr0.5 and Zr1 ribbons in DW are higher than those in MB solution respectively, due to a certain amount of H^+ and methylene blue molecules in the MB solution. The R_{total} (total resistance) of the Zr0,

Zr0.5 and Zr1 ribbons in DW is higher than that in MB solution, and the R_{total} of Zr0.5 and Zr1 ribbons are higher than that of Zr0 ribbon in either DW or MB solution. Thus, the EIS results are also in good agreement with the results of polarization curves (Figure 5a,b).

Table 2. Parameters from EIS measurements: R_s, solution resistance; Q_f and R_f, resistance of passivation film; Q_a and R_a, resistance of electrochemical reaction; R_{total}, total resistance.

Solution	Alloy	R_s ($\Omega \cdot cm^2$)	Q_f		R_f ($\Omega \cdot cm^2$)	Q_a		R_a ($\Omega \cdot cm^2$)	R_{total} ($\Omega \cdot cm^2$)
			Y_f ($\Omega^{-1} \cdot s^{-n} \cdot cm^{-2}$)	N_f		Y_a ($\Omega^{-1} \cdot s^{-n} \cdot cm^{-2}$)	N_a		
DW	Zr0	95.3	5.3×10^{-9}	0.99	895.7	5.2×10^{-9}	0.98	511.0	1502.0
	Zr0.5	125.7	3.4×10^{-9}	0.99	1932.2	3.5×10^{-8}	0.85	593.0	2650.9
	Zr1	147.6	7.8×10^{-9}	0.95	2842.3	8.7×10^{-9}	0.99	716.4	3706.3
MO	Zr0	18.3	4.8×10^{-8}	0.99	211.2	3.4×10^{-5}	0.91	28.4	257.9
	Zr0.5	21.1	3.9×10^{-8}	0.98	250.7	3.0×10^{-5}	0.92	33.7	305.5
	Zr1	24.5	3.8×10^{-8}	0.99	274.7	2.5×10^{-5}	0.93	39.3	338.5

3.5. Effect of pH on Ribbon Degradation

The working pH range of the Fenton-like reaction using the as-spun Zr0, Zr0.5 and Zr1 ribbons for the MB solution degradation has been studied, and keep other reaction conditions constant: T = 298 K, C_{H2O2} = 1 mM, ribbon dosage = 0.5 g L^{-1} and C_{MB} = 100 mg L^{-1}. The highest degradation rate for as-spun Zr0, Zr0.5 and Zr1 ribbons is achieved at pH =3, as shown in Figure 6a–c, respectively. Surprisingly, as pH = 2, the degradation efficiency ($\eta = (1 - C_t/C_0 \times 100\%$, t = 15 min) of as-spun Zr0, Zr0.5 and Zr1 ribbons is lower than that at pH = 3 (Figure 6d). This may be because the iron in the ribbon dissolved to generate hydrogen when the H^+ in the solution is too high ($H^+ + Fe^0 \rightarrow Fe^{2+} + H_2 \uparrow$). This hydrogen evolution reaction generates a large amount of Fe^{2+}, which may consume •OH and lower the oxidation capability of the MB solution (Fe^{2+} + •OH → OH^- + Fe^{3+}). As pH > 3, the η of the MB solution decreases with the increasing pH, as there must be enough H^+ in the solution to carry out Fenton-like reactions. When the pH increases to 4, this MB solution hardly degrades before 7 min, and then it degrades slowly. As pH > 5 the η of MB solution is nearly zero.

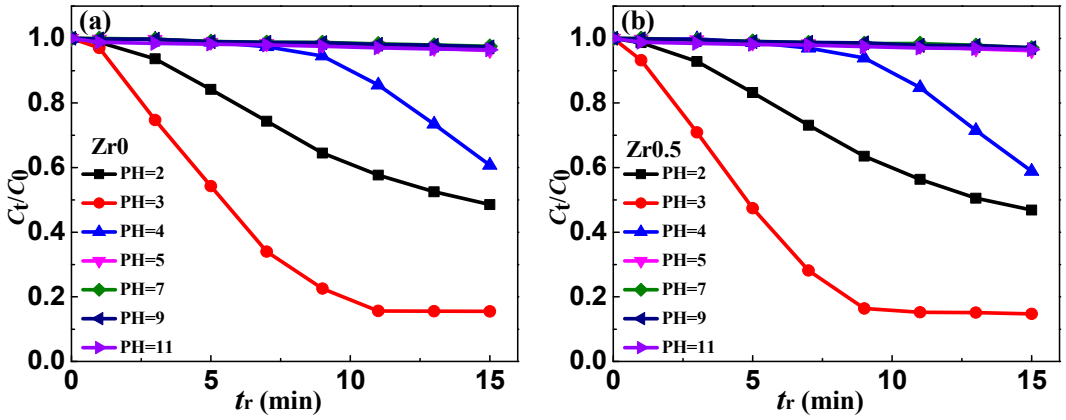

Figure 6. *Cont.*

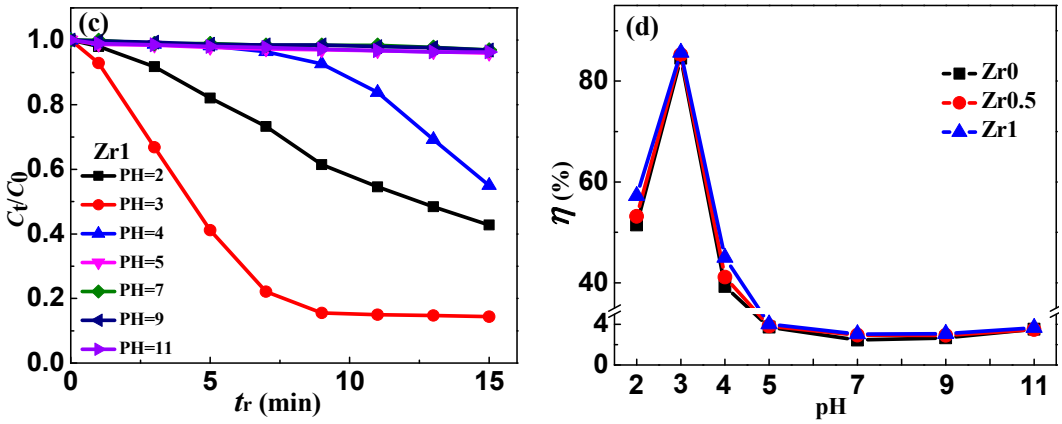

Figure 6. The normalized concentration C_t/C_0 change of MB solution during the degradation process of the as-spun (**a**) Zr0, (**b**) Zr0.5 and (**c**) Zr1 ribbons at different pH values. (**d**) The degradation efficiency ($\eta = (1 - C_t/C_0 \times 100\%$, t = 15 min) of the degradation process vs. pH for Zr0, Zr0.5 and Zr1 ribbons.

3.6. Effect of H_2O_2 Concentration on Ribbon Degradation and Surface Morphology

The concentration of H_2O_2 controls the rate of •OH generation in the Fenton-like reactions. The effect of the concentration on the degradation process of MB solution using as-spun Zr0, Zr0.5 and Zr1 ribbons was investigated, as shown in Figure 7. Various concentrations of H_2O_2, including 0, 0.5, 1, 5, 10, 30 and 50 mM, are added to MB solution, and other reaction conditions constant: T = 298 K, pH = 3, ribbon dosage = 0.5 g L^{-1} and C_{MB} = 100 mg L^{-1}. It is proved that H_2O_2 is necessary to degrade MB solution, because the η is very low without adding H_2O_2 (Figure 7d). When the C_{H2O2} is 0.5 mM, the concentration of MB solution remained basically unchanged after 7 min of degradation, which may be due to the fact that H_2O_2 was completely consumed and •OH could not be produced in Fenton-like reaction. With the C_{H2O2} increasing from 1 to 10 mM, the η of Fe-based ribbons increases gradually. When the C_{H2O2} increases to 30 and 50 mM, the η of MB solution began to decrease significantly. The results show that the appropriate addition of H_2O_2 can effectively accelerate the degradation process. However, due to the well-known hydroxyl radical scavenging effect, excessive H_2O_2 is not beneficial to the degradation process (H_2O_2 + •OH → H_2O + •HO_2). The oxidation potential of generated radical •HO_2 is much lower than that of •OH, which slows the degradation rate of MB solution.

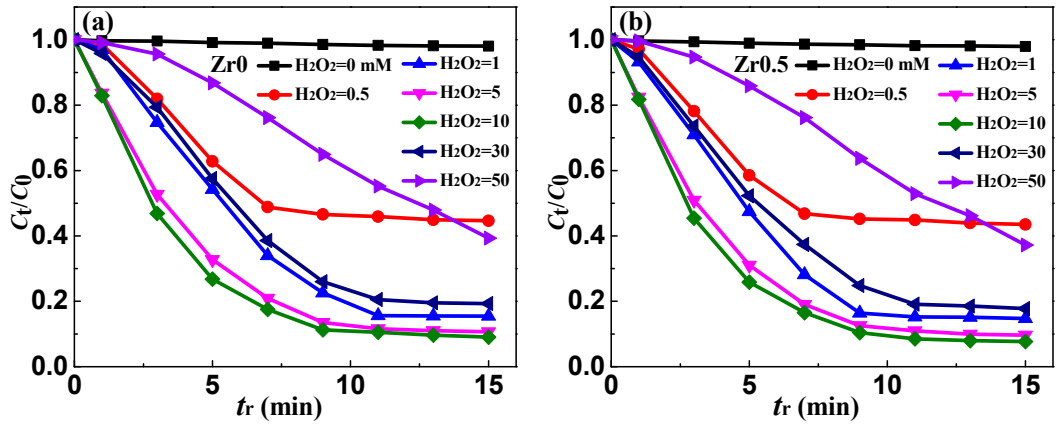

Figure 7. *Cont.*

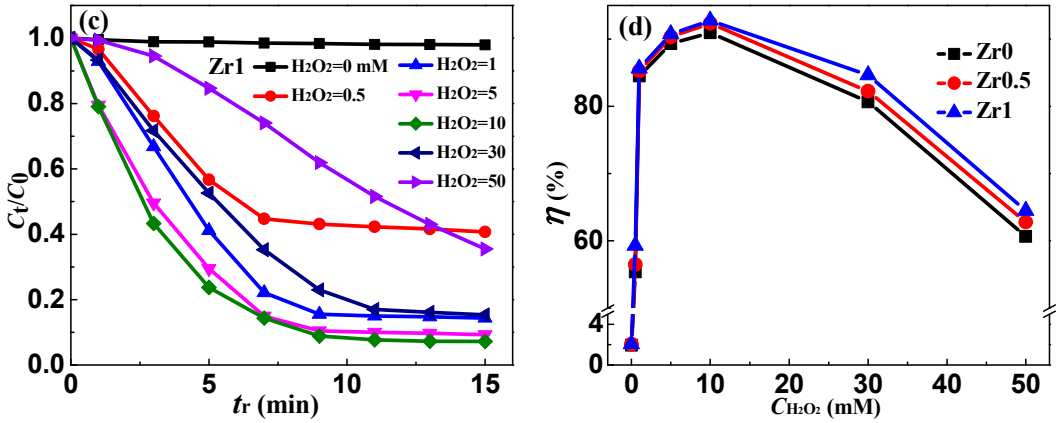

Figure 7. The normalized concentration C_t/C_0 change of MB solution during the degradation process of the as-spun (**a**) Zr0, (**b**) Zr0.5 and (**c**) Zr1 ribbons at different H_2O_2 concentration. (**d**) The degradation efficiency ($\eta = (1 - C_t/C_0 \times 100\%$, t = 15 min) of the degradation process vs. C_{H2O2} for Zr0, Zr0.5 and Zr1 ribbons.

Figure 8 shows the SEM images of as-spun Zr1 ribbon reacted with MB solution at different H_2O_2 concentrations. The surface of the as-spun Zr1 ribbon is relatively smooth (Figure 4c), but fuzzy 3D nano-porous structures appear on the surface of the ribbon as $C_{H_2O_2}$ = 0 mM (Figure 8a). With the $C_{H_2O_2}$ increasing from 0.5 to 5 mM, the 3D nano-porous structures develop and coarsen (Figures 4f and 8b,c). As $C_{H_2O_2}$ = 10 mM, the 3D nano-porous structure begins to transform into an intersecting grid-like structure (Figure 8d). When the $C_{H_2O_2}$ reaches 30 and 50 mM, the intersecting grid-like structure gradually becomes thicker and more developed (Figure 8e,f). Table 3 summarizes the EDS results of the Zr1 ribbon reacted with MB solution at different H_2O_2 concentrations. Comparing the EDS results of the as-spun and reacted Zr1 ribbons ($C_{H_2O_2}$ = 1 mM, Table 1), the Fe content decrement on Zr1 ribbon surface increases gradually with increasing $C_{H_2O_2}$, the c_{Si} and c_B have remained basically unchanged simultaneously. However, the c_O rise on the surface of the Zr1 ribbons increases gradually, which is due to H_2O_2 having strong oxidizability. Excessive H_2O_2 will oxidize the metal on the ribbon surface, resulting in a large number of oxides.

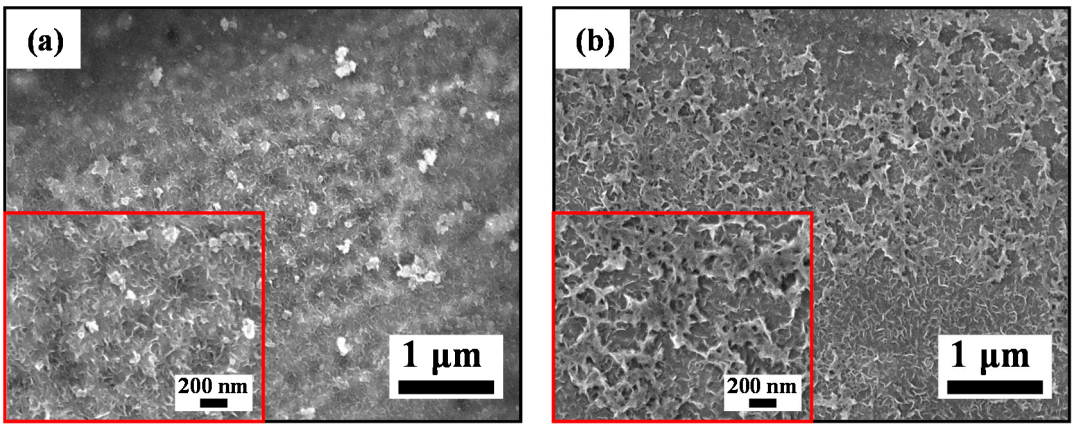

Figure 8. *Cont.*

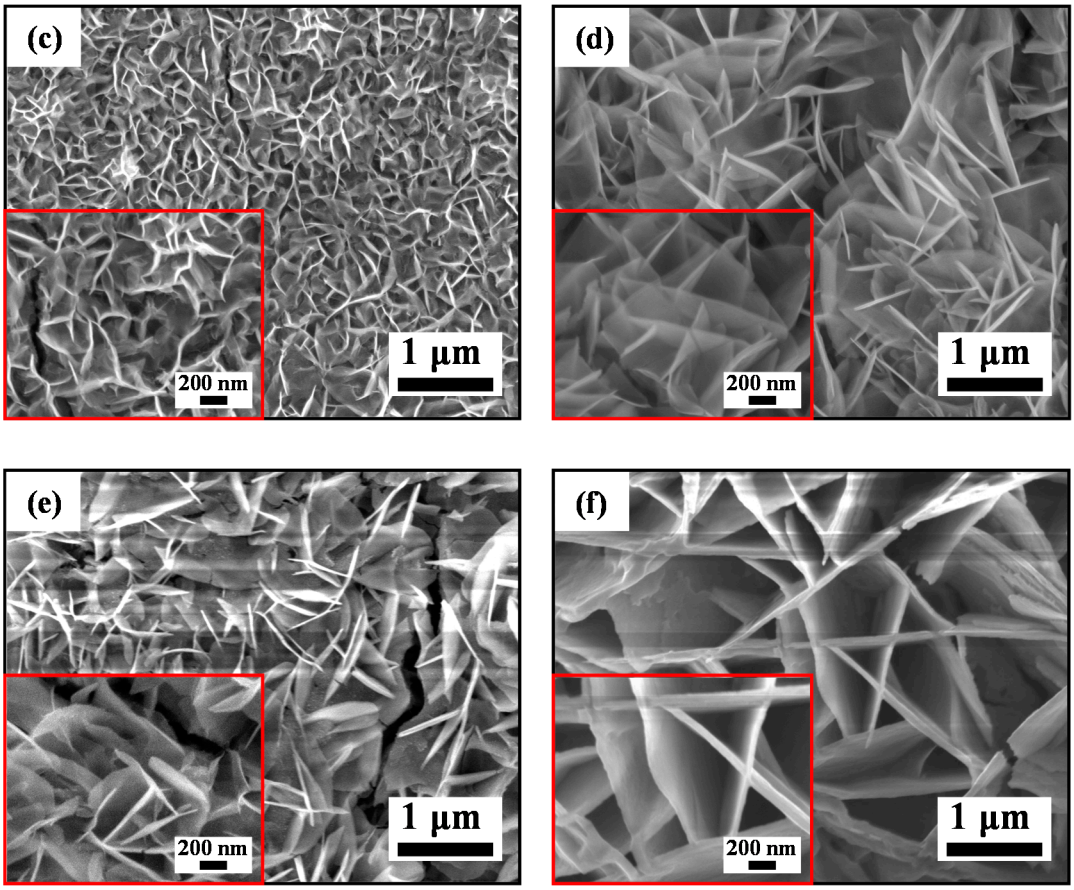

Figure 8. SEM micrographs of (**a**) H_2O_2 = 0 mM, (**b**) H_2O_2 = 0.5 mM, (**c**) H_2O_2 = 5 mM, (**d**) H_2O_2 = 10 mM, (**e**) H_2O_2 = 30 mM and (**f**) H_2O_2 = 50 mM for the as-spun Zr1 ribbons after reacted with MB solution. The insets in (**a**–**f**): the high-magnification images.

Table 3. EDS analysis of the Zr1 ribbon reacted with MB solution at different H_2O_2 concentrations (at.%).

Element	C_{H2O2} (mM)					
	0	**0.5**	**5**	**10**	**30**	**50**
c_{Fe}	69.7	61.1	47.2	43.9	36.4	29.5
c_{Si}	8.3	8.5	8.7	8.1	8.6	8.8
c_{B}	9.6	10.8	9.2	9.9	9.7	9.5
c_{Zr}	1.5	1.4	1.7	1.6	1.4	1.3
c_{O}	10.9	18.2	33.2	36.5	43.9	50.9

4. Discussion

With increasing c_{Zr}, the $2\theta_{max}$ of Fe-based ribbons decreases gradually. Based on the element date [43], the average atomic radius $\bar{r}$ of Zr0, Zr0.5 and Zr1 ribbons is 1.301, 1.302 and 1.303 Å, respectively. According to the equation on the characteristic distance [44–46]:

$$\delta_c = \frac{2\pi}{Q_P}, \text{ with } Q_P = (4\pi \sin\theta_{max})/\lambda, \quad (3)$$

where δ_c is the characteristic distance, Q_P is the diffraction vector of the diffusive maximum of the XRD pattern, and the λ is the X-ray wavelength (Cu-Kα = 1.5418 Å). The δ_c value of as-spun Zr0, Zr0.5 and Zr1 ribbons is 2.036, 2.042 and 2.050 Å, respectively. Here, the $\frac{\bar{r}_{Zr0.5}}{\bar{r}_{Zr0}}$ and $\frac{\bar{r}_{Zr1}}{\bar{r}_{Zr0}}$ equal 1.00077 and 1.00154;

meanwhile, $\frac{\delta_{c,Zr0.5}}{\delta_{c,Zr0}}$ and $\frac{\delta_{c,Zr1}}{\delta_{c,Zr0}}$ equal 1.00295 and 1.00688, which are much higher than the corresponding $\bar{r}$ radius. The high $\frac{\delta_{c,Zr1}}{\delta_{c,Zr0}}$ suggest that Zr atom can introduce free volume into the glassy matrix [47]. On the other hand, Zr atom can enhance the stability of Fe-Zr and Fe-B bonds in the liquid state and glassy state, according to the lower T_{P3} and higher T_{P1}, T_{P2} than those of Zr0 ribbon. It is known that Fe-B can form the network in the Fe-based glasses [48]. Thus, it is expected that the corrosion resistance deduced from potential dynamic scans of the as-spun Zr0.5 and Zr1 ribbons is higher than that of the as-spun Zr0 ribbon (Figure 5). It is understood that the free volume in as-spun Zr0.5 and Zr1 ribbons is higher than the as-spun Zr0 ribbon.

With increasing c_{Zr}, the as-spun Zr0, Zr0.5 and Zr1 amorphous ribbons have gradually increased degradation rate of MB solution (Figure 3d), indicating an increased exciting ability in Fenton-like reaction. The as-spun Zr0, Zr0.5 and Zr1 amorphous ribbons formed the cotton floc structure, coarse porous structure and 3D nano-porous structure on the ribbon surfaces during Fenton-like reaction with MB solution (Figure 4d–f), respectively. Obviously, the 3D nano-porous structure formed on the surface of Zr1 ribbon has a larger specific surface area, which can provide more reactive sites, thus improving the degradation performance of Zr1 ribbon to MB solution. According to DSC curves and electrochemical tests, the higher resistance and T_{P1}, T_{P2} of Zr0.5 and Zr1 ribbon can keep the network, i.e., ligaments of the ribbons, being more stable than Zr0 ribbon. On the other hand, the δ_c value of reacted Zr0, Zr0.5 and Zr1 ribbons is 2.031, 2.035 and 2.039 Å, respectively, and the δ_c decrement values ($\Delta\delta_c$) of Zr0, Zr0.5 and Zr1 ribbons after reaction are 0.005, 0.007 and 0.011 Å, respectively. These data indicate that the free volumes have segregated and fromed the pores on the surface of the ribbons. Hence, it is understood that the pore size increases simultaneously.

Under different C_{H2O2}, the Zr0, Zr0.5 and Zr1 ribbons have different η values in MB solution and have a maximal η as C_{H2O2} = 10 mM (Figure 7d). Meanwhile, in the range of C_{H2O2} = 0.5–30 mM, the η of Zr0.5 and Zr1 ribbons is higher than Zr0 ribbon, indicating that the existence of Zr element would slow down the change of η in wide C_{H2O2} range. As C_{H2O2} is 1 mM, the amount and size of acicular Fe-based oxides on Zr1 ribbon surface are higher than on the Zr0 surface. Hence, the interface of Fe_xO_y/matrix on Zr0 ribbon surface is more compatible than on Zr1 ribbon surface, indicating that the Fe atom below the Zr1 ribbon surface can move to the outer layer more easily than on the Zr0 ribbon surface. In addition, under the help of the porous structure, the specific surface area of the Zr1 ribbon is higher and the η is higher than Zr0 ribbon. As C_{H2O2} reaches 30 mM, the amount and size of Fe_xO_y are very high, and cover the pore mouth and inhibit the inner Fe atom transport to the surface to join Fenton-like reaction. This explains why the η of Fe-based ribbons decreases as C_{H2O2} increases from 30 mM.

Based on the analysis of the elemental information, surface micro-morphology and micro-structure of Zr0 and Zr1 amorphous ribbons during MB solution (T = 298 K, pH = 3, C_{H2O2} = 1 mM and C_{MB} = 100 mg L^{-1}) degradation, the pathway of this Fenton-like reaction can be drawn, as shown schematically in Figure 9. According to δ_c of as-spun Zr0 and Zr1 ribbons, the free volume in Zr1 ribbon is higher Zr0 ribbon. In the reaction process, the Fe atoms can diffuse under the help of free volume and more to the surface to join the Fenton-like reaction to degrade the MB solution. At the same time, the free volume can segregate to form the pore in the reaction. Meanwhile, T_{P1} and T_{P2} of the Zr1 ribbon is higher than that of the Zr0 ribbon, which can make the network in the glassy matrix more stable. Hence, the ligament is more easily formed in the reacted Zr1 ribbon. Moreover, Fe_xO_y is not compatible with ligaments and leave the channel active, which helps iron atoms to transport toward the surface from the inner part of the ribbon matrix. Hence, the Zr1 ribbon has a higher η and k than Zr0 ribbon under the same condition. These results not only prove that Zr1 amorphous ribbon has high degradability to organic dyes, but also reveal that Zr element has the role of tunnel construction in Fe-based alloys.

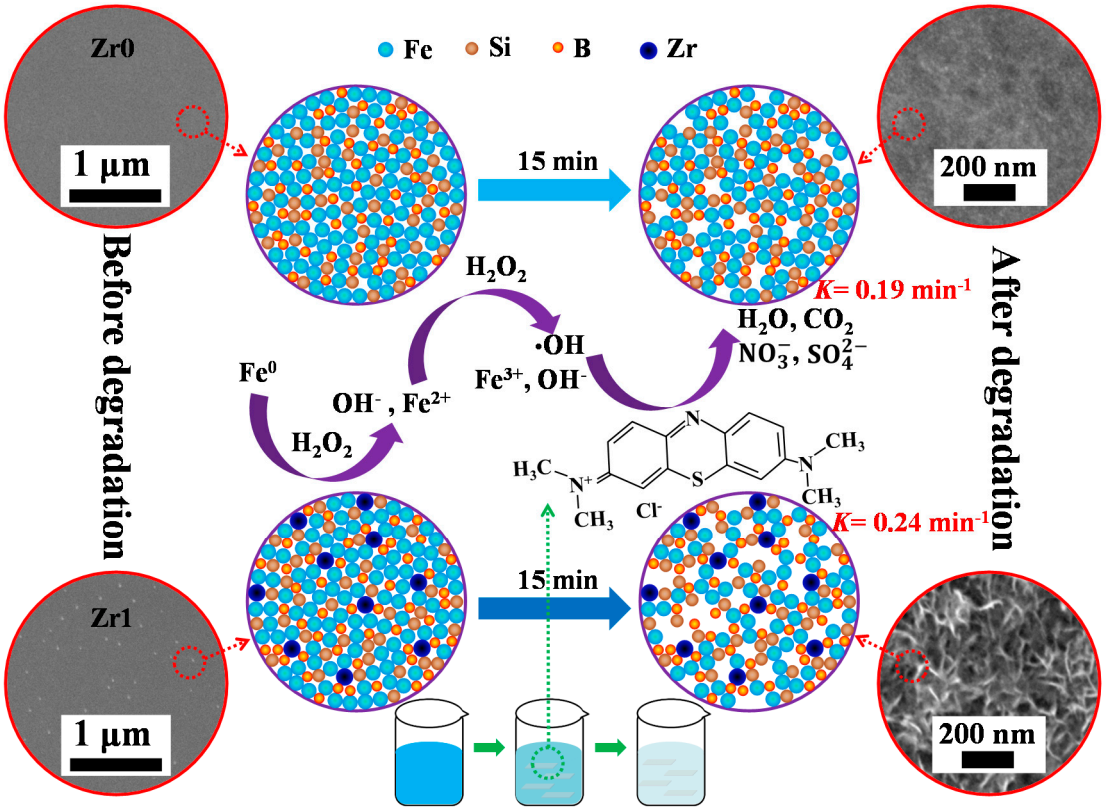

Figure 9. Schematic diagrams of the pathway of MB solution degradation in Fenton-like reaction using the Zr0 and Zr1 amorphous ribbons.

5. Conclusions

In this work, we have prepared Zr0, Zr0.5 and Zr1 amorphous ribbons with melt-spun method and we studied the microstructure, MB solution degradation behavior with several technologies. With increasing c_{Zr}, the as-spun Zr0, Zr0.5 and Zr1 amorphous ribbons have gradually increased degradation rate of MB solution. According to δ_c of as-spun Zr0, Zr0.5 and Zr1 ribbons, the free volume in Zr1 ribbon is higher for Zr0 and Zr0.5 ribbons. In the reaction process, the 3D nano-porous structure formed on the surface of Zr1 ribbon has a higher specific surface area than the cotton floc structure formed by Zr0 ribbon and coarse porous structure formed by Zr0.5 ribbon. We prove that the high free volume makes it easy to form a pore structure in the reaction process, and the construction of these tunnels is beneficial to the transport of iron atoms inner the ribbon to the surface. Thus, the Zr1 ribbon has high η and k than Zr0 and Zr0.5 ribbons under the same condition. The nonmonotonic influence of pH value and H_2O_2 concentration on the degradation η and k of Zr1 ribbon is similar to Zr0 and Zr0.5 ribbons. This work not only provides a new method for the remediation of organic dye wastewater, but also extends the application prospect of Fe-based amorphous alloys.

Author Contributions: Conceptualization, Q.C. and Z.Y.; methodology, Q.C. and H.Z.; investigation, Q.C. and L.-C.Z.; data curation, H.M. and W.W. (Wenlong Wang); writing—original draft preparation, Q.C.; writing—review and editing, Q.C. and W.W. (Weimin Wang); supervision, L.-C.Z. and W.W. (Weimin Wang). All authors have read and agreed to the published version of the manuscript.

Funding: This research was funded by the National Key Research Program of China, grant number 2016YFB0300501, National Natural Science Foundation of China, grant number 51471099, 51571132, 51511140291 and 51771103, Key R&D Plan of Shandong Province grant number grant number 2019GGX102016.

Conflicts of Interest: The authors declare no conflict of interest.

References

1. Lachheb, H.; Puzenat, E.; Houas, A.; Ksibi, M.; Elaloui, E.; Guillard, C.; Herrmann, J.M. Photocatalytic degradation of various types of dyes (Alizarin S, Crocein Orange G, Methyl Red, Congo Red, Methylene Blue) in water by UV-irradiated titania. *Appl. Catal. B* **2002**, *39*, 75–90. [CrossRef]
2. Fu, F.L.; Dionysiou, D.D.; Liu, H. The use of zero-valent iron for groundwater remediation and wastewater treatment: A review. *J. Hazard. Mater.* **2014**, *267*, 194–205. [CrossRef] [PubMed]
3. Park, H.; Choi, W. Visible light and Fe(III)-mediated degradation of Acid Orange 7 in the absence of H_2O_2. *J. Photochem. Photobiol. A* **2003**, *159*, 241–247. [CrossRef]
4. Djilani, C.; Zaghdoudi, R.; Djazi, F.; Bouchekima, B.; Lallam, A.; Modarressi, A.; Rogalski, M. Adsorption of dyes on activated carbon prepared from apricot stones and commercial activated carbon. *J. Taiwan Inst. Chem. Eng.* **2015**, *53*, 112–121. [CrossRef]
5. Pawar, R.R.; Gupta, P.; Sawant, S.Y.; Shahmoradi, B.; Lee, S.M. Porous synthetic hectorite clay-alginate composite beads for effective adsorption of methylene blue dye from aqueous solution. *Int. J. Biol. Macromol.* **2018**, *114*, 1315–1324. [CrossRef] [PubMed]
6. Nigam, P.; Banat, I.M.; Singh, D.; Marchant, R. Microbial process for the decolorization of textile effluent containing azo, diazo and reactive dyes. *Process Biochem.* **1996**, *31*, 435–442. [CrossRef]
7. Lucas, M.; Peres, J. Decolorization of the azo dye Reactive Black 5 by Fenton and photo-Fenton oxidation. *Dyes Pigm.* **2006**, *71*, 236–244. [CrossRef]
8. Shende, A.G.; Tiwari, C.S.; Bhoyar, T.H.; Vidyasagar, D.; Umare, S.S. BWO nano-octahedron coupled with layered g-C_3N_4: An efficient visible light active photocatalyst for degradation of cationic/anionic dyes, and N_2 reduction. *J. Mol. Liq.* **2019**, *296*, 111771. [CrossRef]
9. Tan, W.B.; Wang, L.; Yu, H.X.; Zhang, H.; Zhang, X.H.; Jia, Y.F.; Li, T.T.; Dang, Q.L.; Cui, D.Y.; Xi, B.D. Accelerated microbial reduction of azo dye by using biochar from iron-rich-biomass pyrolysis. *Materials* **2019**, *12*, 1079. [CrossRef] [PubMed]
10. Zhang, Y.Z.; Liu, J.F.; Chen, D.; Qin, Q.D.; Wu, Y.; Huang, F.; Li, W. Preparation of FeOOH/Cu with high catalytic activity for degradation of organic dyes. *Materials* **2019**, *12*, 338. [CrossRef]
11. Shen, W.J.; Kang, H.L.; Ai, Z.H. Comparison of aerobic atrazine degradation with zero valent aluminum and zero valent iron. *J. Hazard. Mater.* **2018**, *357*, 408–414. [CrossRef] [PubMed]
12. Gupta, N.K.; Ghaffari, Y.; Bae, J.; Kim, K.S. Synthesis of coral-like α-Fe_2O_3 nanoparticles for dye degradation at neutral pH. *J. Mol. Liq.* **2020**, *301*, 112473. [CrossRef]
13. Bhatt, C.S.; Nagaraj, B.; Suresh, A.K. Nanoparticles-shape influenced high-efficient degradation of dyes: Comparative evaluation of nano-cubes vs nano-rods vs nano-spheres. *J. Mol. Liq.* **2017**, *242*, 958–965. [CrossRef]
14. Li, X.N.; Li, J.H.; Shi, W.L.; Bao, J.F.; Yang, X.Y. A Fenton-like nanocatalyst based on easily separated magnetic nanorings for oxidation and degradation of dye pollutant. *Materials* **2020**, *13*, 332. [CrossRef] [PubMed]
15. Tara, N.; Arslan, M.; Hussain, Z.; Iqbal, M.; Khan, Q.M.; Afzal, M. On-site performance of floating treatment wetland macrocosms augmented with dye-degrading bacteria for the remediation of textile industry wastewater. *J. Clean. Prod.* **2019**, *217*, 541–548. [CrossRef]
16. Lin, B.; Bian, X.F.; Wang, P.; Luo, G.P. Application of Fe-based metallic glasses in wastewater treatment. *Mater. Sci. Eng. B* **2012**, *177*, 92–95. [CrossRef]
17. Zhang, C.Q.; Zhu, Z.W.; Zhang, H.F.; Hu, Z.Q. Rapid reductive degradation of azo dyes by a unique structure of amorphous alloys. *Chin. Sci. Bull.* **2011**, *56*, 3988–3992. [CrossRef]
18. Zhang, L.C.; Kim, K.B.; Yu, P.; Zhang, W.Y.; Kunz, U.; Eckert, J. Amorphization in mechanically alloyed (Ti, Zr, Nb)-(Cu, Ni)-Al equiatomic alloys. *J. Alloys Compd.* **2007**, *428*, 157–163. [CrossRef]
19. Zhao, Y.F.; Si, J.J.; Song, J.G.; Yang, Q.; Hui, X.D. Synthesis of Mg-Zn-Ca metallic glasses by gas-atomization and their excellent capability in degrading azo dyes. *Mater. Sci. Eng. B* **2014**, *181*, 46–55. [CrossRef]
20. Wang, J.Q.; Liu, Y.H.; Chen, M.W.; Louzguine-Luzgin, D.V.; Inoue, A.; Perepezko, J.H. Excellent capability in degrading azo dyes by MgZn-based metallic glass powders. *Sci. Rep.* **2012**, *2*, 418. [CrossRef]
21. Chen, Q.; Pang, J.; Yan, Z.C.; Hu, Y.H.; Guo, L.Y.; Zhang, H.; Zhang, L.C.; Wang, W.M. MgZn-based amorphous ribbon as a benign decolorizer in methyl blue solution. *J. Non Cryst. Solids* **2020**, *529*, 119802. [CrossRef]

22. Chen, Q.; Yan, Z.C.; Guo, L.Y.; Zhang, H.; Zhang, L.C.; Kim, K.; Li, X.Y.; Wang, W.M. Enhancing the acid orange dye degradation efficiency of Mg-based glassy alloys with introducing porous structure and zinc oxide. *J. Alloys Compd.* **2020**, *831*, 154817. [CrossRef]
23. Zhang, C.Q.; Zhu, Z.W.; Zhang, H.F. Mg-based amorphous alloys for decolorization of azo dyes. *Results Phys.* **2017**, *7*, 2054–2056. [CrossRef]
24. Shaheen, K.; Suo, H.L.; Shah, Z.; Khush, L.; Arshad, T.; Khan, S.B.; Siddique, M.; Ma, L.; Liu, M.; Cui, J.; et al. Ag-Ni and Al-Ni nanoparticles for resistive response of humidity and photocatalytic degradation of methyl orange dye. *Mater. Chem. Phys.* **2020**, *244*, 122748. [CrossRef]
25. Das, S.; Garrison, S.; Mukherjee, S. Bi-functional mechanism in degradation of toxic water pollutants by catalytic amorphous metals. *Adv. Eng. Mater.* **2016**, *18*, 214–218. [CrossRef]
26. Wang, P.P.; Wang, J.Q.; Li, H.; Yang, H.; Huo, J.T.; Wang, J.G.; Chang, C.T.; Wang, X.M.; Li, R.W.; Wang, G. Fast decolorization of azo dyes in both alkaline and acidic solutions by Al-based metallic glasses. *J. Alloys Compd.* **2017**, *701*, 759–767. [CrossRef]
27. Sha, Y.Y.; Mathew, I.; Cui, Q.Z.; Clay, M.; Gao, F.; Zhang, X.Q.J.; Gu, Z.Y. Rapid degradation of azo dye methyl orange using hollow cobalt nanoparticles. *Chemosphere* **2016**, *144*, 1530–1535. [CrossRef]
28. Mondal, A.; Adhikary, B.; Mukherjee, D. Room-temperature synthesis of air stable cobalt nanoparticles and their use as catalyst for methyl orange dye degradation. *Colloids Surf.* **2015**, *482*, 248–257. [CrossRef]
29. Taneja, P.; Sharma, S.; Umar, A.; Mehta, S.K.; Ibhadon, A.O.; Kansal, S.K. Visible-light driven photocatalytic degradation of brilliant green dye based on cobalt tungstate ($CoWO_4$) nanoparticles. *Mater. Chem. Phys.* **2018**, *211*, 335–342. [CrossRef]
30. Wang, J.Q.; Liu, Y.H.; Chen, M.W.; Xie, G.Q.; Louzguine Luzgin, D.V.; Inoue, A.; Perepezko, J.H. Rapid degradation of Azo dye by Fe-based metallic glass powder. *Adv. Funct. Mater.* **2012**, *22*, 2567–2570. [CrossRef]
31. Wang, Q.Q.; Chen, M.X.; Lin, P.H.; Cui, Z.Q.; Chu, C.G.; Shen, B.L. Investigation of FePC amorphous alloys with self-renewing behaviour for highly efficient decolorization of methylene blue. *J. Mater. Chem. A* **2018**, *6*, 10686–10699. [CrossRef]
32. Liu, P.; Zhang, J.L.; Zha, M.Q.; Shek, C.H. Synthesis of an Fe rich amorphous structure with a catalytic effect to rapidly decolorize Azo dye at room temperature. *ACS Appl. Mater. Interfaces* **2014**, *6*, 5500–5505. [CrossRef] [PubMed]
33. Zhang, L.C.; Jia, Z.; Lyu, F.; Liang, S.X.; Lu, J. A review of catalytic performance of metallic glasses in wastewater treatment: Recent progress and prospects. *Prog. Mater. Sci.* **2019**, *105*, 100576. [CrossRef]
34. Liang, S.X.; Jia, Z.; Liu, Y.J.; Zhang, W.C.; Wang, W.M.; Lu, J. Compelling rejuvenated catalytic performance in metallic glasses. *Adv. Mater.* **2018**, *30*, 1802764. [CrossRef]
35. Jia, Z.; Zhang, W.C.; Wang, W.M.; Habibi, D.; Zhang, L.C. Amorphous $Fe_{78}Si_9B_{13}$ alloy: An efficient and reusable photo-enhanced Fenton-like catalyst in degradation of cibacron brilliant red 3B-A dye under UV-vis light. *Appl. Catal. B* **2016**, *192*, 46–56. [CrossRef]
36. Liang, S.X.; Wang, X.Q.; Zhang, W.C.; Liu, Y.J.; Wang, W.M.; Zhang, L.C. Selective laser melting manufactured porous Fe-based metallic glass matrix composite with remarkable catalytic activity and reusability. *Appl. Mater. Tod.* **2020**, *19*, 100543. [CrossRef]
37. Jia, Z.; Liang, S.X.; Zhang, W.C.; Wang, W.M.; Yang, C.; Zhang, L.C. Heterogeneous photo Fenton-like degradation of cibacron brilliant red 3B-A dye using amorphous $Fe_{78}Si_9B_{13}$ and $Fe_{73.5}Si_{13.5}B_9Cu_1Nb_3$ alloys: The influence of adsorption. *J. Taiwan Inst. Chem. Eng.* **2017**, *71*, 128–136. [CrossRef]
38. Jia, Z.; Kang, J.; Zhang, W.C.; Wang, W.M.; Yang, C.; Sun, H.; Habibi, D.; Zhang, L.C. Surface aging behaviour of Fe-based amorphous alloys as catalysts during heterogeneous photo Fenton-like process for water treatment. *Appl. Catal. B* **2017**, *204*, 537–547. [CrossRef]
39. Xie, S.; Huang, P.; Kruzic, J.J.; Zeng, X.; Qian, H. A highly efficient degradation mechanism of methyl orange using Fe-based metallic glass powders. *Sci. Rep.* **2016**, *6*, 21947. [CrossRef]
40. Tschopp, M.A.; Horstemeyer, M.F.; Gao, F.; Sun, X.; Khaleel, M. Energetic driving force for preferential binding of self-interstitial atoms to Fe grain boundaries over vacancies. *Scr. Mater.* **2011**, *64*, 908–911. [CrossRef]
41. Nam, S.; Tratnyek, P.G. Reduction of azo dyes with zero-valent iron. *Water Res.* **2000**, *34*, 1837–1845. [CrossRef]
42. Jia, C.G.; Pang, J.; Pan, S.P.; Zhang, Y.J.; Kim, K.B.; Qin, J.Y.; Wang, W.M. Tailoring the corrosion behavior of Fe-based metallic glasses through inducing Nb-triggered netlike structure. *Corros. Sci.* **2019**, *147*, 94–107. [CrossRef]

43. Li, G.H.; Wang, W.M.; Bian, X.F.; Zhang, J.T.; Li, R.; Wang, L. Comparing the dynamic and thermodynamic behaviors of $Al_{86}Ni_9$-La_5/$(La_{0.5}Ce_{0.5})_5$ amorphous alloys. *J. Alloys Compd.* **2009**, *478*, 745–749. [CrossRef]
44. Guo, L.Y.; Wang, X.; Shen, K.C.; Kim, K.B.; Lan, S.; Wang, X.L.; Wang, W.M. Structure modification and recovery of amorphous $Fe_{73.5}Si_{13.5}B_9Nb_3Cu_1$ magnetic ribbons after autoclave treatment: SAXS and thermodynamic analysis. *J. Mater. Sci. Technol.* **2019**, *35*, 118–126. [CrossRef]
45. Sokolov, A.P.; Kisliuk, A.; Soltwisch, M.; Quitmann, D. Medium-range order in glasses: Comparison of Raman and diffraction measurements. *Phys. Rev. Lett.* **1992**, *69*, 1540–1542. [CrossRef]
46. Wang, W.M.; Zhang, W.X.; Gebert, A.; Roth, S.; Mickel, C.; Schultz, L. Microstructure and Magnetic Properties in $Fe_{61}Co_{9-x}Zr_8Mo_5W_xB_{17}$ ($0 \leq \times \leq 3$) Glasses and Glass-Matrix Composites. *Metall. Mater. Trans. A* **2009**, *40*, 511–521. [CrossRef]
47. Yavari, A.R.; Moulec, A.L.; Inoue, A.; Nishiyama, N.; Lupu, N.; Matsubara, E.; Botta, W.J.; Vaughan, G.; Michiel, M.D.; Kvick, Å. Excess free volume in metallic glasses measured by X-ray diffraction. *Acta Mater.* **2005**, *53*, 1611–1619. [CrossRef]
48. Muneyuki, I.; Shigeo, S.; Hisato, K.; Matsubara, E.; Inoue, A. Crystallization behavior of amorphous $Fe_{90-X}Nb_{10}B_X$ (X = 10 and 30) alloys. *Mater. Trans.* **2000**, *11*, 1526–1529.